

Hipandas: Hyperspectral Image Joint Denoising and Super-Resolution by Image Fusion with the Panchromatic Image

Shuang Xu^{1,2}, Zixiang Zhao³, Haowen Bai⁴, Chang Yu⁴, Jiangjun Peng^{1,2}, Xiangyong Cao⁴, Deyu Meng⁴

¹ Northwestern Polytechnical University,

² Research & Development Institute of Northwestern Polytechnical University in Shenzhen,

³ ETH Zürich, ⁴ Xi'an Jiaotong University

Abstract

*Hyperspectral images (HSIs) are frequently noisy and of low resolution due to the constraints of imaging devices. Recently launched satellites can concurrently acquire HSIs and panchromatic (PAN) images, enabling the restoration of HSIs to generate clean and high-resolution imagery through fusing PAN images for denoising and super-resolution. However, previous studies treated these two tasks as independent processes, resulting in accumulated errors. This paper introduces **Hyperspectral Image Joint Pandenoising and Pansharpening (Hipandas)**, a novel learning paradigm that reconstructs HRHS images from noisy low-resolution HSIs (LRHS) and high-resolution PAN images. The proposed zero-shot Hipandas framework consists of a guided denoising network, a guided super-resolution network, and a PAN reconstruction network, utilizing an HSI low-rank prior and a newly introduced detail-oriented low-rank prior. The interconnection of these networks complicates the training process, necessitating a two-stage training strategy to ensure effective training. Experimental results on both simulated and real-world datasets indicate that the proposed method surpasses state-of-the-art algorithms, yielding more accurate and visually pleasing HRHS images.*

1. Introduction

Hyperspectral imaging has emerged as a powerful tool in remote sensing [29]. Nevertheless, the acquisition of hyperspectral images (HSIs) is often impeded by practical limitations. Factors such as atmospheric turbulence and limited sensor apertures commonly result in noise corruption and low spatial resolution for HSIs.

Denoising [50, 51] and super-resolution [5, 8, 33] have been developed to enhance the quality. In contrast to single-image restoration, the fusion of auxiliary images from other modalities potentially leads to improve-

ment. The recent launch of satellites equipped with hyperspectral-panchromatic (HS-PAN) imaging systems, e.g. the PRISMA satellite, presents a new opportunity. PAN images, distinguished by their high spatial resolution and lack of noise, serve as an ideal data source for fusion [9, 12].

As illustrated in Fig. 1(a) and (b), guided denoising and super-resolution can be achieved through pansharpening and pandenoising techniques, respectively. However, the images captured by HS-PAN satellites (e.g. PRISMA) are typically noisy and of low resolution. Currently, enhancing image quality requires sequentially applying pandenoising and pansharpening to noisy low-resolution HS (NLRHS) images. This sequential strategy poses several challenges:

- Denoising and super-resolution are treated as independent steps, requiring highly precise algorithms for both pandenoising and pansharpening. Inadequate denoising can lead to noise amplification during super-resolution.
- Denoising may inadvertently smooth essential details, thereby complicating texture recovery for the super-resolution process.
- The inherent interdependence of denoising and super-resolution implies that their disjoint execution may not fully exploit their synergistic potential.

In response to the challenges, as shown in Fig. 1(c), the study explores a novel technique named **Hyperspectral Image Joint Pandenoising and Pansharpening (Hipandas)**, designed to reconstruct clean HRHS images from NLRHS inputs, fused with high-resolution PAN (HRPAN) images. Since real-world satellites tend to produce noisy and low-resolution HSIs, the Hipandas task is more aligned with practical scenarios than pandenoising or pansharpening tasks alone. Due to the lack of large-scale datasets for the Hipandas task, a zero-shot learning method is proposed. This method comprises a guided denoising network, a guided super-resolution network, and a PAN reconstruction network. The first two networks are utilized for image enhancement, while the third ensures modality fidelity. These networks are interconnected, with the outputs of the upstream networks serving as inputs to the down-

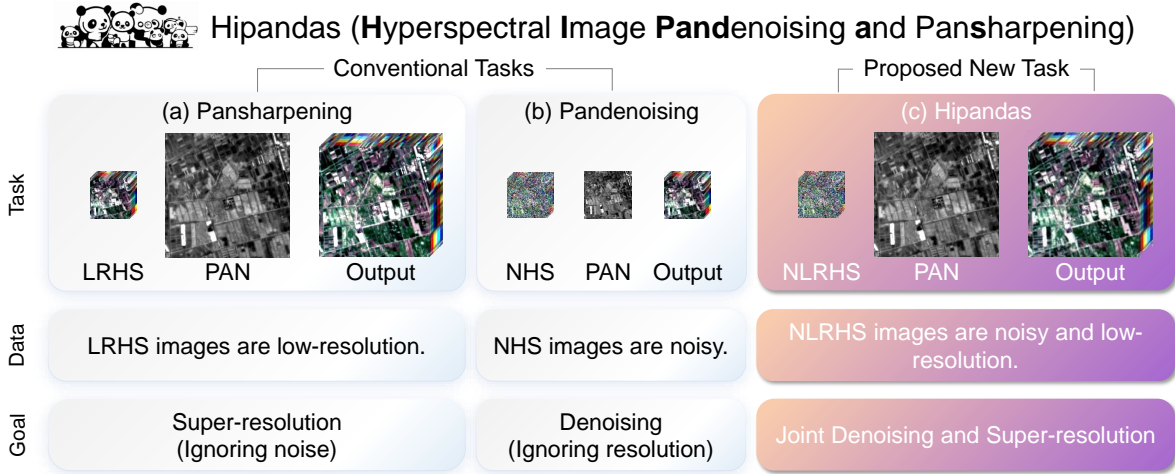


Figure 1. The differences among (a) pansharpening, (b) pandoising and (c) Hipandas. Pansharpening addresses super-resolution, while pandoising focuses on denoising. In contrast, Hipandas is specifically designed to tackle both problems in a unified framework.

stream networks, thereby complicating the training process. Consequently, a two-stage training strategy is introduced. It is initially pretrained on low-resolution images and then finetuned on high-resolution images to mitigate learning bias towards the noise. Empirical results indicate that the two-stage training strategy overwhelmingly outperforms the one-stage strategy. In summary, the contributions are as follows:

- This paper proposes the Hipandas task, which is more aligned with practical scenarios. A *zero-shot learning-based Hipandas (ZSHipandas)* is formulated for this task.
- A detail-oriented low-rank prior is introduced for the Hipandas task and is applied to the network architecture design of ZSHipandas.
- A two-stage training strategy is proposed to effectively train ZSHipandas, which yields more accurate and visually appealing HRHS images compared to state-of-the-art (SOTA) methods.

The organization of this paper is as follows. Section 2 reviews related work. Section 3 delves into the detailed description of the proposed Hipandas method. Section 4 reports experimental results. Section 5 concludes the paper.

2. Related Work

2.1. HSI super-resolution and pansharpening

Before deep learning, techniques such as sparse coding [1, 43], wavelets [27], and Gaussian processes [2] were employed for single HSI super-resolution. The success of deep RGB image super-resolution [6] led to the emergence of convolutional neural networks (CNNs) as a powerful tool in the domain of single HSI super-resolution. This includes 3D CNNs [18, 23], spectral information preserv-

ing networks [14, 20], spatial-spectral prior-based networks [15, 37], and diffusion-based networks [24, 39, 41, 42].

Despite the achievements, the fusion of additional modalities has the potential to yield better results [36]. PAN images, characterized by the high spatial resolution and signal-to-noise ratio, serve as effective guides [4, 22, 34]. Qu *et al.* developed a 3D CNN to fuse HS-PAN information [31]. Dong *et al.* implemented adversarial learning for spectrum preserved HS-PAN fusion [7]. Guarino *et al.* introduced a rolling pansharpening CNN (RPNN) using band-wise training to address challenges such as limited training data and variations of band number [10]. Li *et al.* proposed a dual conditional diffusion models-based fusion network that operates in an iterative denoising manner [19]. Rui *et al.* introduced a low-rank diffusion model for hyperspectral pansharpening (PLRD), taking the strengths of a pretrained diffusion model for enhanced generalization [32].

2.2. HSI denoising and pandoising

For HSI denoising, a range of techniques have been developed, including total variation [28, 38], nuclear norm [30, 35, 49] and subspace methods [13]. In the era of deep learning, CNNs [3, 40, 47] and transformers [16, 17, 25] have demonstrated promise. More recently, diffusion models have emerged as effective tools in HSI denoising. Zeng *et al.* utilized a transformer-based backbone for spectral unmixing, with abundance maps denoised using a self-supervised generative diffusion network [48]. Pang *et al.* developed a unified HSI restoration network based on diffusion models (HIRD), which reconstructs clean HSI data from the product of two low-rank components, employing a pretrained diffusion model for base image sampling [26].

Extensive research has been conducted on single HSI de-

Table 1. Main notations in this paper.

Variable	Denotation
P	High-resolution PAN (HRPAN) image
Q	Low-resolution PAN (LRPAN) image
H	High-resolution HS (HRHS) image
L	Low-resolution HS (LRHS) image
N	Noisy LRHS (NLRHS) image

noising, but there is a lack of work on pandenoising. To the best of our knowledge, the study by Xu *et al.* [45] represents the sole study on this topic. Based on the assumption that PAN and HS images share similar textures, Xu *et al.* proposed a PAN-weighted total variation (PWTV) regularization [45]. Fusing PAN images enables PWTV to outperform single HSI denoising methods.

2.3. Hipandas

Pansharpening aims to improve spatial resolution, while pandenoising is devoted to remove noise. However, real-world satellites tend to produce noisy and low-resolution imagery, and sequential implementations of pansharpening and pandenoising is at the risk of accumulated errors. To the best of our knowledge, this paper is the early exploration on end-to-end HSI denoising and super-resolution by image fusion with PAN images.

3. Zero-Shot Hipandas

This section proposes the Hipandas technique, and main notations are summarized in Tab. 1.

3.1. Problem formulation for Hipandas

In HS imaging, the acquired data tends to be noisy and of low resolution, which can be modeled by corrupting the downsampled HRHS image with noise ε , $N = H \downarrow + \varepsilon$, where $N \in \mathbb{R}^{h \times w \times b}$ and $H \in \mathbb{R}^{sh \times sw \times b}$ are the noisy LRHS and HRHS images, respectively, and \downarrow is the down-sampling operation. Here, s denotes the ratio of spatial resolution, h , w , and b denote the height, width and band number, respectively. For the HS-PAN imaging device, the system also acquires HRPAN images $P \in \mathbb{R}^{sh \times sw}$.

PAN images, which offers complementary information, make PAN-guided HSI restoration a promising technique for achieving high-fidelity HSIs. This study introduces a method termed *Hyperspectral Image Joint Pandenoising and Pansharpening (Hipandas)*, which aims to reconstruct the noise-free HRHS image H from an NLRHS image N fused with the HRPAN image P .

3.2. Proposed method

Due to the limited availability of large-scale datasets with paired images $\{N, P, H\}$, this study proposes a *zero-shot learning framework for Hipandas (ZSHipandas)*. As depicted in Fig. 2, ZSHipandas consists of three components:

a Guided Denoising Network (GDN), a Guided Super-Resolution Network (GSRN), and a Panchromatic Reconstruction Network (PRN).

The GDN component is designed to eliminate noise from the LRHS image N , with the guidance of the PAN image to produce a denoised LRHS image \hat{L} . Given that the observed PAN image P possesses a higher spatial resolution than N , the GDN component employs the LRPAN image $Q = P \downarrow$ to align with the spatial resolution of N . This process is formalized as

$$\hat{L} = \text{GDN}(N, Q). \quad (1)$$

The GSRN component improves spatial resolution through a detail injection approach. Initially, \hat{L} is upsampled (*e.g.*, via bicubic interpolation) to generate a coarse HRHS image. Subsequently, $\hat{L} \uparrow$ and P restore the missing details, and the final HRHS image \hat{H} is expressed as

$$\hat{H} = \text{GSRN}(\hat{L}, P) = \hat{L} \uparrow + f(\hat{L} \uparrow, P), \quad (2)$$

where $f(\hat{L} \uparrow, P)$ represents the predicted detail map. In addition to the aforementioned guidance during the restoration process, the strong relationship between PAN and HS images can provide valuable information. Consequently, the PRN component is employed to ensure that PAN images can be reconstructed from HSIs, formalized as

$$\hat{P} = \text{PRN}(\hat{H}), \quad \hat{Q} = \text{PRN}(\hat{L}), \quad (3)$$

where \hat{P} and \hat{Q} denote the reconstructed PAN images.

3.3. Loss functions and training details

The joint training of the three networks presents specific challenges:

- The training data consists solely of the NLRHS image N , HRPAN image P , and LRPAN image Q . Lacking ground truth supervision, the formulation of rational loss functions is crucial for the training of ZSHipandas.
- The output of the GDN component is utilized as the input for the GSRN component. However, during the early steps of training, the GDN component cannot generate a satisfactorily denoised image, which would introduce a training bias towards noise in the GSRN’s training.

To mitigate these problems, loss functions tailored to the three networks are proposed, accompanied by a two-stage training strategy:

Stage 1. In this stage, the networks are pretrained at the LR scale. The reasons are twofold. LR scale images can reduce computational burden. Additionally, neural networks’ spectral bias property implies that training on LR images is less complex than on HR ones [46].

a) For the GDN component, to achieve robust denoising, an ℓ_1 loss is utilized instead of the ℓ_2 one between the NLRHS image N and the denoised LRHS image $\hat{L} =$

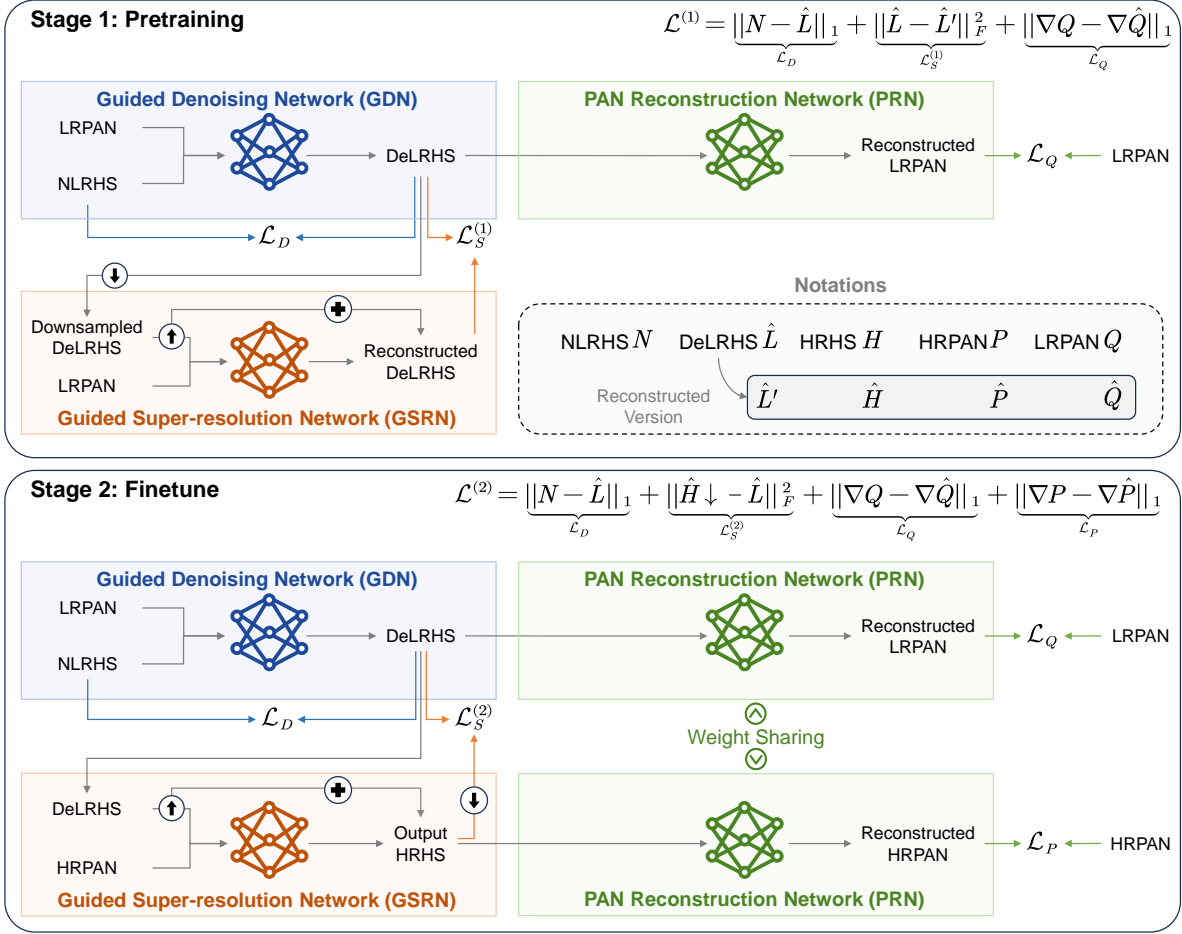


Figure 2. The framework for the proposed ZSHipandas. It is pretrained in stage 1 on LR scale images, and then finetuned in stage 2 on HR scale images. The GDN and GSRN components are used for image enhancement, while the PRN component models relationship between HS and PAN images.

GDN (N, Q), as expressed by

$$\mathcal{L}_D = \|N - \hat{L}\|_1. \quad (4)$$

b) For the PRN component, it is imperative that the reconstructed LRPAN image maintains textures. By revising the total variation regularization, this goal is achieved by the PAN image’s high-frequency information loss,

$$\mathcal{L}_Q = \|\nabla Q - \nabla \hat{Q}\|_1, \quad (5)$$

where ∇ represents the Sobel operator.

c) For the GSRN component, which involves super-resolution, the network cannot be trained on the observed dataset since there is no HR-LR image pair. Thus, the denoised LRHS image $\hat{L} \in \mathbb{R}^{h \times w \times b}$ is deemed as the HR data, and its downsampled version $\hat{L} \downarrow \in \mathbb{R}^{h/s \times w/s \times b}$ is regarded as the LR data. Then, the image could be reconstructed by $\hat{L}' = \text{GSRN}(\hat{L} \downarrow, Q) \in \mathbb{R}^{h \times w \times b}$. In this way, \hat{L} can be used as ground truth, and it compels the GSRN

component to learn the recovery of lost details by

$$\mathcal{L}_S^{(1)} = \|\hat{L} - \hat{L}'\|_F^2. \quad (6)$$

In summary, the loss function in stage 1 is:

$$\mathcal{L}^{(1)} = \mathcal{L}_D + \mathcal{L}_S^{(1)} + \mathcal{L}_Q. \quad (7)$$

Stage 2. In this stage, the networks are finetuned with weights initialized from the pretraining phase. The loss functions \mathcal{L}_D and \mathcal{L}_Q remain unchanged. However, the objective of the GSRN component in this stage is to reconstruct an HRHS image, denoted as $\hat{H} = \text{GSRN}(\hat{L}, P)$. In the absence of a ground truth HRHS image to supervise the learning of detail reconstruction, it has to ensure that the downsampled HRHS image retains the same content as the LRHS image. Consequently, the loss function for the GSRN component is defined as

$$\mathcal{L}_S^{(2)} = \|\hat{H} \downarrow - \hat{L}\|_F^2. \quad (8)$$

Furthermore, given that the HRHS image has been reconstructed in this stage, a PAN image’s high-frequency information loss is also introduced at the HR scale:

$$\mathcal{L}_P = \|\nabla P - \nabla \hat{P}\|_1. \quad (9)$$

In summary, the loss function in stage 2 is:

$$\mathcal{L}^{(2)} = \mathcal{L}_D + \mathcal{L}_S^{(2)} + \mathcal{L}_Q + \mathcal{L}_P. \quad (10)$$

3.4. Network structure

It is important to incorporate data prior into network structures. The low-rank nature of HSIs is well-established and widely applied in HSI denoising. However, the prior for HSI pansharpening is less explored. As Eq. (2) is based on the detail injection framework, the focus of this paper is on modeling the prior for the detail obtained by $f(\cdot, \cdot)$.

Low-rank Prior for detail maps. The detail represents the information lost from an LRHS image during its reconstruction to an HRHS image. Given an HRHS image H , when downsampled to $L = H \downarrow$ and subsequently upsampled to $L \uparrow$, the clean detail map is derived as $D = H - L \uparrow$. Accounting for noise, the practical detail is the noisy version, $\tilde{D} = H - N \uparrow$, where $N = H \downarrow + \varepsilon$.

One of the main contributions of the work is the identification of the detail map D as being inherently low-rank. This insight is based on an analysis of the energy curves for both clean and noisy detail maps. The k -th energy value is computed as $\sum_{i=1}^k \lambda_i / \sum_{i=1}^b \lambda_i$, where λ_i represents the singular value of the detail map. A steeper energy curve signifies a higher degree of low-rankness in the corresponding detail map. Through simulations of noisy detail maps corrupted by Gaussian or mixed noise at varying intensities, as depicted in Fig. 3, it is observed that the clean detail map exhibits a stronger low-rank characteristic, whereas the noisy detail map tends to disrupt this property. Thus, incorporating the low-rank prior of the detail map into the network $f(\cdot, \cdot)$ facilitates the recovery of more accurate detail maps.

Network designing. For GDN and GSRN components, their architectures are designed as a guided low-rank matrix factorization network, leveraging low-rank priors for both HSIs and detail maps. As depicted in Fig. 4(a), the network output is represented as the product of two factor matrices. Taking the GDN component as an instance, the denoised HSI is expressed as $\hat{L} = V \times_3 U$, where \times_3 denotes the mode-3 product, $V \in \mathbb{R}^{h \times w \times r}$ constitutes r base images, and $U \in \mathbb{R}^{b \times r}$ represents the expression coefficients. Specifically, the i -th band of \hat{L} is a linear combination of r base images, given by $\hat{L}_{:,i} = \sum_{k=1}^r U_{i,k} V_{:,i,k}$. By setting $r \ll b$, the model enforces a low-rank structure on network outputs.

Conventional matrix factorization models typically address the optimization problem, $\min_{U,V} \{\mathcal{L}(Y, V \times_3 U) +$

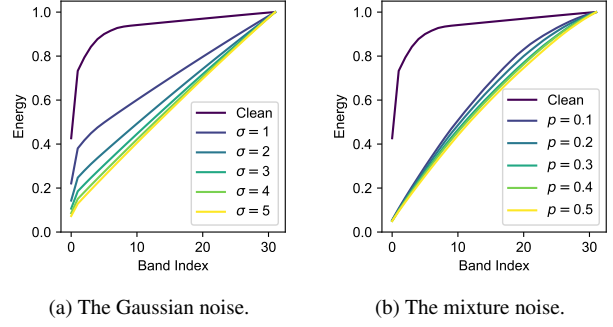


Figure 3. The energy curve of clean and corrupted detail maps (i.e., D and \tilde{D}). σ and p denote the noise intensity for Gaussian and mixture noise, respectively.

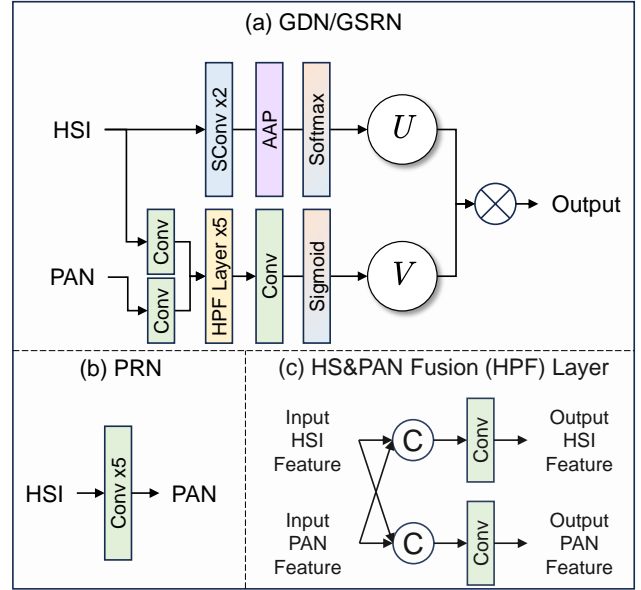


Figure 4. The architecture for the (a) GDN/GSRN component, (b) PRN component and (c) HPF layer. Conv and SConv denote convolutional and strided convolutional units, respectively. AAP denotes the adaptive average pooling.

$\mathcal{R}_1(V) + \mathcal{R}_2(U)\}$, where Y denotes the noisy observation, and $\mathcal{L}(\cdot, \cdot)$ and $\mathcal{R}_i(\cdot)$ denote the loss and regularization functions, respectively. The estimations of U and V are computed via iterative algorithms and expressed as functions of the observed data. However, this approach is heavily reliant on manually designed objective functions.

In contrast, this work parametrizes V and U as functions of the observation data via neural networks, with the forward propagation of the network approximating the computational flow of iterative algorithms by the data-driven manner, thereby potentially obviating the need for hand-crafted objective functions.

The proposed architecture comprises two distinct branches. The U -branch models spectral information. It applies 2 strided convolution (SConv) units to the HSI, each

Table 2. Averaged metrics on simulated data between ground truth H and restored image \hat{H} for the Hipandas task in Gaussian noise cases, where σ denotes the intensity of Gaussian noise. Best and second-best values are **highlighted** and underlined.

Methods	i.i.d. Gaussian ($\sigma = 10$)				i.i.d. Gaussian ($\sigma = 30$)				non-i.i.d. Gaussian ($\sigma \in [10, 50]$)			
	PSNR \uparrow	SSIM \uparrow	ERGAS \downarrow	SAM \downarrow	PSNR \uparrow	SSIM \uparrow	ERGAS \downarrow	SAM \downarrow	PSNR \uparrow	SSIM \uparrow	ERGAS \downarrow	SAM \downarrow
PLRD+HIRD	37.93	0.9229	11.97	4.61	28.40	0.6866	31.04	10.78	27.89	0.7499	30.92	13.37
PLRD+PWTV	34.53	0.7881	17.11	7.23	27.42	0.5212	37.73	17.46	28.84	0.6198	35.44	19.81
SwinIR+HIRD	29.89	0.8569	52.50	7.90	29.80	0.8497	31.98	8.62	28.10	0.8267	43.11	16.08
SwinIR+PWTV	27.93	0.6855	212.50	13.16	18.63	0.1659	984.41	44.46	19.60	0.2446	966.29	44.54
RPNN+HIRD	36.60	0.9280	12.43	4.53	32.11	0.8711	19.98	7.28	32.43	0.8765	19.68	8.06
RPNN+PWTV	37.19	0.9342	12.27	4.31	29.73	0.6570	27.38	12.85	31.37	0.7440	26.13	13.25
HIRD+PLRD	34.36	0.8308	450.92	8.34	27.60	0.6303	569.13	19.14	26.99	0.5976	557.02	31.35
HIRD+SwinIR	36.24	0.8904	13.15	3.61	34.09	0.8700	16.65	5.40	32.20	0.8603	20.17	8.12
HIRD+RPNN	37.40	0.9314	11.95	4.10	35.06	0.9194	15.61	5.74	33.03	0.9072	18.97	8.22
PWTV+PLRD	36.56	0.9059	13.65	4.88	34.09	0.8865	18.21	7.20	32.48	0.8777	21.49	10.07
PWTV+SwinIR	37.65	0.9080	11.18	<u>3.09</u>	34.15	0.8393	16.53	5.38	34.26	0.8370	17.71	6.33
PWTV+RPNN	<u>38.34</u>	<u>0.9415</u>	<u>10.88</u>	3.87	<u>36.70</u>	0.9314	<u>13.20</u>	<u>4.76</u>	<u>36.70</u>	<u>0.9299</u>	<u>13.46</u>	<u>4.97</u>
ZSHipandas (ours)	40.61	0.9547	8.50	3.00	36.88	<u>0.9271</u>	12.35	4.63	37.24	0.9313	11.87	4.52

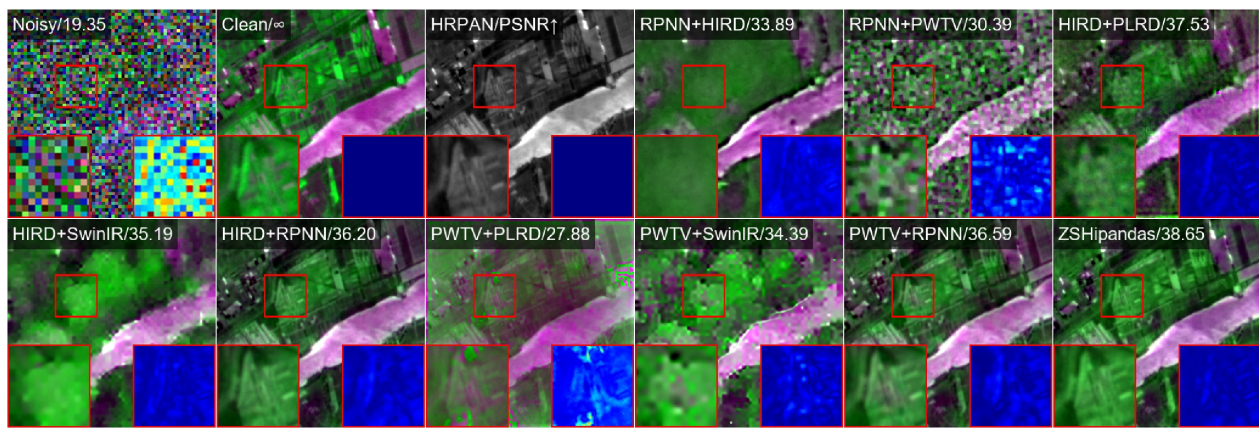


Figure 5. Restoration results for Gaussian noise with $\sigma = 30$.

reducing the spatial resolution by a factor of two, resulting in a feature of size $h/4 \times w/4 \times b$. An adaptive average pooling operation is applied along the spatial dimensions, followed by a softmax activation, to yield the transposed coefficient matrix $U^T \in \mathbb{R}^{r \times b}$. The V -branch is designed to generate base images. Since PAN and base images share similar structures, PAN and HS images are fused in this net. It begins with 2 head convolution (Conv) units that embed both HS and PAN images into shallow features with identical channels. Five HS and PAN fusion (HPF) layers are then utilized, with a tail Conv unit transforming the deep HS feature into V with r channels, activated by a sigmoid function. To mitigate computational intensity, the HPF layer is designed with a simple structure, comprising two separate Conv units applied to the concatenated HS and PAN features to produce the output features. Throughout this paper, all Conv or SConv units are activated by leaky rectified linear units, unless otherwise specified.

As for the PRN component, it is commonly postulated

that there exists a spectral transform matrix $\Phi \in \mathbb{R}^{1 \times B}$, which characterizes the spectral degradation between PAN-HS imaging [11, 44], expressed as $P = H \times_3 \Phi$. However, this does not hold true for numerous satellite systems. The PRN component thus is designed as 5 stacked Conv units.

4. Experiments

4.1. Results on simulated datasets

Datasets. Acquiring paired NLRHS, HRHS and HRPAN images is challenging, so NLRHS and HRPAN images are simulated from HRHS images. A 32-band clean HSI captured over Dongying, Shandong, China, by the Zhuhai-1 satellite, is selected. This image is divided into 81 patches of 256×256 pixels, which are regarded as HRHS images H . The corresponding NLRHS images N are obtained by $N = H \downarrow + \varepsilon$, leading to images with a size of $64 \times 64 \times 32$. The HRPAN image P is synthesized by applying the spectral response function of the IKONOS satellite to H .

Noise configuration. The first group comprises three

Table 3. Averaged metrics on simulated data between ground truth H and restored image \hat{H} for the Hipandas task in mixture noise cases, where p denotes the intensity of mixture noise. Best and second-best values are **highlighted** and underlined.

Methods	Mixture ($p = 0.15$)				Mixture ($p = 0.35$)				Mixture ($p = 0.55$)			
	PSNR \uparrow	SSIM \uparrow	ERGAS \downarrow	SAM \downarrow	PSNR \uparrow	SSIM \uparrow	ERGAS \downarrow	SAM \downarrow	PSNR \uparrow	SSIM \uparrow	ERGAS \downarrow	SAM \downarrow
PLRD+HIRD	29.38	0.8394	26.88	12.84	28.81	0.8275	28.55	13.04	28.20	0.7876	<u>34.12</u>	13.80
PLRD+PWTV	30.54	0.7028	32.25	18.27	29.70	0.6709	34.25	18.85	28.45	0.6183	85.80	21.01
SwinIR+HIRD	29.73	0.8410	37.83	11.66	29.38	0.8335	42.06	12.44	29.11	0.8255	51.47	13.60
SwinIR+PWTV	25.05	0.4912	766.41	37.41	23.80	0.4505	821.29	38.79	22.15	0.3873	1415.73	39.44
RPNN+HIRD	33.87	0.8931	17.47	6.90	32.75	0.8798	21.79	8.40	31.94	0.8656	31.09	<u>9.86</u>
RPNN+PWTV	34.91	0.8537	19.38	9.50	32.64	0.8045	24.91	11.98	30.71	0.7371	76.43	14.97
HIRD+PLRD	28.27	0.6445	605.39	34.60	29.18	0.6677	543.26	28.21	24.99	0.5323	561.31	41.36
HIRD+SwinIR	32.28	0.8628	20.69	8.77	31.91	0.8582	24.04	9.62	31.61	0.8500	36.18	10.81
HIRD+RPNN	33.11	0.9071	19.41	8.84	32.72	0.9037	22.84	9.68	32.44	0.8970	35.26	10.88
PWTV+PLRD	32.42	0.8689	24.60	11.72	31.86	0.8595	27.06	13.10	31.37	0.8512	38.51	13.67
PWTV+SwinIR	36.64	0.8855	14.52	5.25	35.77	0.8749	16.83	6.01	33.42	0.8255	335.51	11.53
PWTV+RPNN	<u>37.79</u>	<u>0.9372</u>	<u>12.11</u>	<u>4.51</u>	<u>37.20</u>	<u>0.9336</u>	<u>13.71</u>	<u>5.18</u>	<u>35.41</u>	<u>0.9035</u>	194.38	10.30
ZSHipandas (ours)	40.24	0.9541	9.07	3.23	38.66	0.9448	10.79	3.91	36.61	0.9227	45.26	8.68

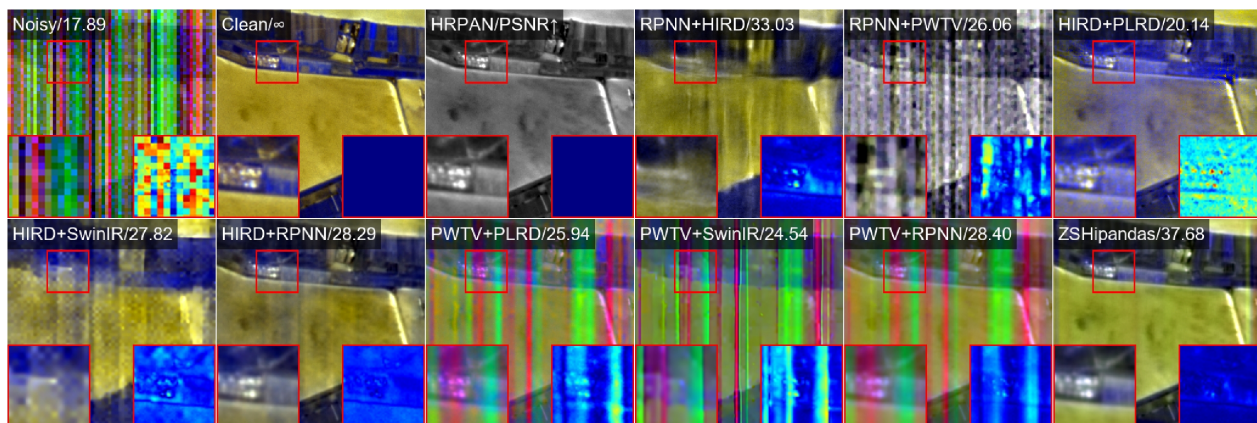


Figure 6. Restoration results for mixture noise with $p = 0.55$.

scenarios: independent and identically distributed (i.i.d.) Gaussian noise with $\sigma = 10$ and 30, and non-i.i.d. Gaussian noise with $\sigma \in [10, 50]$. The second group involves mixed noise, where non-i.i.d. Gaussian noise affects 2/3 bands, and impulse, stripe and deadline noise affect 1/3 bands with intensities of $p = 0.15, 0.35$, and 0.55.

Evaluate metrics. Performance is assessed by peak signal-to-noise ratio (PSNR), structural similarity (SSIM), Erreur Relative Globale Adimensionnelle de Synthèse (ERGAS), and spectral angle mapper (SAM). Higher PSNR and SSIM, along with lower ERGAS and SAM, signify better results.

Implement details. Experiments were conducted on a computer with a RTX 3090 GPU. The training comprised two stages, each consisting of 400 and 600 epochs, with the Adam optimizer of a learning rate 10^{-3} . The channel number in networks was fixed at 128. For the GDN and GSRN components, the respective ranks r were set to 3 and 12.

Compared methods. ZSHipandas is compared with SOTA methods including HIRD [26], PWTV [45], SwinIR [21],

PLRD [32], and RPNN [10]. The first two are denoising or pandenoising algorithms, and the others are super-resolution or pansharpening algorithms. They are executed in sequence, and two kinds of execution order are considered: super-resolution+denoising, and denoising+super-resolution.

Quantitative Analysis. Tab. 2 and Tab. 3 present the evaluation metrics for the Gaussian and mixture noise scenarios, respectively. Compared with PWTV+RPNN (the second best method), ZSHipandas could achieve improvement by 2.3 dB for the case of i.i.d. Gaussian noise with $\sigma = 10$, and by 1.3 dB for the case of mixture noise with $p = 0.55$. The data illustrate that our proposed ZSHipandas demonstrates a marked enhancement in performance.

Visual Assessment. Fig. 5 provides a visual comparison of the restoration results for images corrupted by Gaussian noise at an intensity of $\sigma = 30$. It is evident that the images restored by HIRD+SwinIR, PWTV+PLRD, and PWTV+SwinIR still exhibit noticeable noise, and other

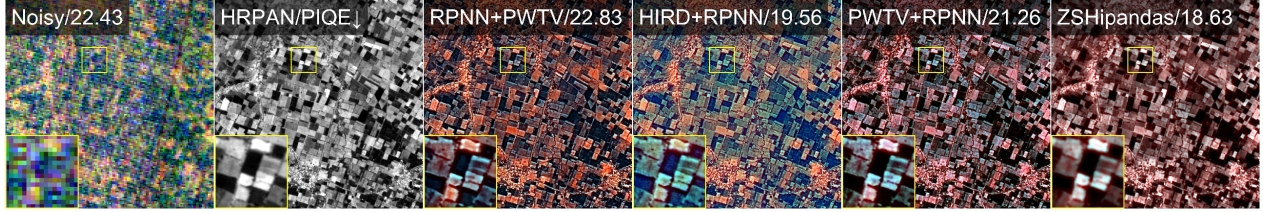


Figure 7. Results on the real-world dataset, Kanpur. PIQE is displayed in the left-upper corner, and lower PIQE indicates better results.

methods suffer from considerable spectral distortion. Fig. 6 depicts the restoration results for images affected by mixture noise at an intensity of $p = 0.55$. It reveals that all the compared methods fail to effectively restore the images, with severe noise remaining and significant details being lost. However, the proposed ZSHipandas consistently exhibits good performance across different cases.

4.2. Results on the real-world dataset

The methods are applied to a real-world dataset which was captured over Kanpur, India, by the PRISMA satellite. The original dataset is very large, so a small patch is cropped. The NLRHS image is of size $144 \times 144 \times 49$, and the HRPAN image is of size 864×864 , where the ratio of spatial resolution is $s = 6$. In this case, RPNN+PWT, HIRD+RPNN and PWT+RPNN are carried out, while many methods are unavailable due to the CUDA out of memory problem. However, these three methods are best performers in simulated experiments, and thus their results are very competitive.

Fig. 7 visualizes the results. The local region marked by the box is amplified in the left-bottom corner. It is shown that the image is severely degraded by the noise with a blue color. Restored images by still preserve the unpleasant color, indicating a spectral distortion. In contrast, ZSHipandas produces a good result with clear textures and satisfactory color. A no-reference metric, Perception based Image Quality Evaluator (PIQE), is reported in Fig. 7; and lower PIQE means better quality. The PIQE values also validate our conclusion.

4.3. Ablation experiments

Ablation experiments are conducted to validate the rationality of the proposed method. Results are listed in Tab. 4 for a noise case, i.i.d. Gaussian noise with $\sigma = 10$.

Three components. To comprehensively evaluate the effectiveness of each component in ZSHipandas, Exp. I-III respectively remove GDN, GSRN and PRN components by deleting the corresponding loss functions. The results indicate that the removal of any component significantly degrades performance, showing the indispensability.

Two-stage training. Exp. IV is the scenario without pre-training to validate the rationality of two-stage training. Results show that direct training cannot yield satisfactory per-

Table 4. Results of six ablation experiments. **Bold** indicates the best value.

	Configurations	PSNR	SSIM	ERGAS	SAM
I	w/o \mathcal{L}_D	19.51	0.5823	57.25	19.51
II	w/o $\mathcal{L}_S^{(1)}$ and $\mathcal{L}_S^{(2)}$	31.49	0.9210	20.37	4.41
III	w/o \mathcal{L}_P and \mathcal{L}_Q	33.32	0.7529	17.44	3.57
IV	w/o pretraining	35.94	0.9284	31.92	4.19
V	w/o low-rank modeling for GDN/GSRN	36.99	0.9325	13.35	3.83
VI	w/o fusion of PAN	33.76	0.7706	16.91	3.54
	Ours	40.61	0.9547	8.50	3.00

Table 5. Evaluation metrics between ground truth L and denoised image \hat{L} for the denoising task in the i.i.d. Gaussian noise case with $\sigma = 10$.

	PSNR	SSIM	ERGAS	SAM
ZSHipandas	41.68	0.9610	7.05	2.32
Only denoising	40.67	0.9522	8.60	2.93

formance, suggesting that pretraining is a critical step in preventing the training bias towards noise.

Low-rank modeling for GDN/GSRN components. The architecture of GDN/GSRN components is based on low-rank priors. Exp. V studies the architecture without low-rank prior by revising it as a plain CNN for the fusion of HS and PAN images. The results show that performance is degraded by 3.6 dB without this prior.

Fusion of PAN images. Exp. VI investigates the scenario without PAN images' fusion. It is evident that this case results in substantial degradation, suggesting the proposed model effectively fuses PAN images.

4.4. Interaction of pandenoising and pansharpening

This subsection evaluates the impact of pansharpening on the performance of pandenoising. To address this, we independently train a GDN component with supervision from \mathcal{L}_D . Subsequently, we compare its denoising capability for LRHS images against ZSHipandas. Tab. 5 illustrates that employing only the GRN component yields a PSNR value of 40.67. However, when denoising and super-resolution are integrated, as in ZSHipandas, there is a 1 dB enhancement in performance, illustrating the synergy between pandenoising and pansharpening. More analysis can be found in supporting information.

5. Conclusion

This paper explores the Hipandas problem for HSI joint restoration by image fusion, which is more practical than

the sequential implementation of pansharpening and pannoising. The proposed ZSHipandas is designed by fully exploiting the HSI and detail low-rank priors. With elaborate loss functions and the two-stage training strategy, ZSHipandas outperforms SOTA methods.

References

- [1] Naveed Akhtar, Faisal Shafait, and Ajmal S. Mian. Bayesian sparse representation for hyperspectral image super resolution. In *CVPR*, pages 3631–3640, 2015. 2
- [2] Naveed Akhtar, Faisal Shafait, and Ajmal S. Mian. Hierarchical beta process with gaussian process prior for hyperspectral image super resolution. In *ECCV*, pages 103–120, 2016. 2
- [3] Xiangyong Cao, Xueyang Fu, Chen Xu, and Deyu Meng. Deep spatial-spectral global reasoning network for hyperspectral image denoising. *IEEE TGRS*, 60:1–14, 2022. 2
- [4] Renwei Dian, Anjing Guo, and Shutao Li. Zero-shot hyperspectral sharpening. *IEEE TPAMI*, 45(10):12650–12666, 2023. 2
- [5] Renwei Dian, Tianci Shan, Wei He, and Haibo Liu. Spectral super-resolution via model-guided cross-fusion network. *IEEE TNNLS*, 35(7):10059–10070, 2024. 1
- [6] Chao Dong, Chen Change Loy, Kaiming He, and Xiaoou Tang. Learning a deep convolutional network for image super-resolution. In *ECCV*, pages 184–199, 2014. 2
- [7] Wenqian Dong, Yufei Yang, Jiahui Qu, Weiying Xie, and Yunsong Li. Fusion of hyperspectral and panchromatic images using generative adversarial network and image segmentation. *IEEE TGRS*, 60:5508413, 2022. 2
- [8] Jian Fang, Jingxiang Yang, Abdolraheem Khader, and Liang Xiao. MIMO-SST: multi-input multi-output spatial-spectral transformer for hyperspectral and multispectral image fusion. *IEEE TGRS*, 62:5510020, 2024. 1
- [9] Pedram Ghamisi, Behnood Rasti, Naoto Yokoya, Qunming Wang, Bernhard Hofle, Lorenzo Bruzzone, Francesca Bovolo, Mingmin Chi, Katharina Anders, Richard Gloaguen, Peter M. Atkinson, and Jon Atli Benediktsson. Multisource and multitemporal data fusion in remote sensing: A comprehensive review of the state of the art. *IEEE Geoscience and Remote Sensing Magazine*, 7(1):6–39, 2019. 1
- [10] Giuseppe Guarino, Matteo Ciotola, Gemine Vivone, and Giuseppe Scarpa. Band-wise hyperspectral image pansharpening using CNN model propagation. *IEEE TGRS*, 62:5500518, 2024. 2, 7
- [11] Jiang He, Jie Li, Qiangqiang Yuan, Huanfeng Shen, and Liangpei Zhang. Spectral response function-guided deep optimization-driven network for spectral super-resolution. *IEEE TNNLS*, 33(9):4213–4227, 2022. 6
- [12] Lin He, Zhou Fang, Jun Li, Jocelyn Chanussot, and Antonio Plaza. Two spectral-spatial implicit neural representations for arbitrary-resolution hyperspectral pansharpening. *IEEE TGRS*, 62:5513621, 2024. 1
- [13] Wei He, Quanming Yao, Chao Li, Naoto Yokoya, Qibin Zhao, Hongyan Zhang, and Liangpei Zhang. Non-local meets global: An iterative paradigm for hyperspectral image restoration. *IEEE TPAMI*, 44(4):2089–2107, 2022. 2
- [14] Jing Hu, Xiuping Jia, Yunsong Li, Gang He, and Minghua Zhao. Hyperspectral image super-resolution via intrafusion network. *IEEE TGRS*, 58(10):7459–7471, 2020. 2
- [15] Junjun Jiang, He Sun, Xianming Liu, and Jiayi Ma. Learning spatial-spectral prior for super-resolution of hyperspectral imagery. *IEEE TCI*, 6:1082–1096, 2020. 2
- [16] Miaoyu Li, Ying Fu, and Yulun Zhang. Spatial-spectral transformer for hyperspectral image denoising. In *AAAI*, pages 1368–1376, 2023. 2
- [17] Miaoyu Li, Ji Liu, Ying Fu, Yulun Zhang, and Dejing Dou. Spectral enhanced rectangle transformer for hyperspectral image denoising. In *CVPR*, pages 5805–5814, 2023. 2
- [18] Qiang Li, Qi Wang, and Xuelong Li. Exploring the relationship between 2d/3d convolution for hyperspectral image super-resolution. *IEEE TGRS*, 59(10):8693–8703, 2021. 2
- [19] Shuangliang Li, Siwei Li, and Lihao Zhang. Hyperspectral and panchromatic images fusion based on the dual conditional diffusion models. *IEEE TGRS*, 61:5526315, 2023. 2
- [20] Yunsong Li, Jing Hu, Xi Zhao, Weiying Xie, and Jiaojiao Li. Hyperspectral image super-resolution using deep convolutional neural network. *Neurocomputing*, 266:29–41, 2017. 2
- [21] Jingyun Liang, Jiezhong Cao, Guolei Sun, Kai Zhang, Luc Van Gool, and Radu Timofte. Swinir: Image restoration using swin transformer. In *ICCVW*, pages 1833–1844, 2021. 7
- [22] Xiaochen Lu, Junping Zhang, Dezheng Yang, Longting Xu, and Fengde Jia. Cascaded convolutional neural network-based hyperspectral image resolution enhancement via an auxiliary panchromatic image. *IEEE TIP*, 30:6815–6828, 2021. 2
- [23] Shaohui Mei, Xin Yuan, Jingyu Ji, Yifan Zhang, Shuai Wan, and Qian Du. Hyperspectral image spatial super-resolution via 3d full convolutional neural network. *Remote. Sens.*, 9(11):1139, 2017. 2
- [24] Yuchun Miao, Lefei Zhang, Liangpei Zhang, and Dacheng Tao. DDS2M: self-supervised denoising diffusion spatio-spectral model for hyperspectral image restoration. In *ICCV*, pages 12052–12062, 2023. 2
- [25] Li Pang, Weizhen Gu, and Xiangyong Cao. Trq3dnet: A 3d quasi-recurrent and transformer based network for hyperspectral image denoising. *Remote. Sens.*, 14(18):4598, 2022. 2
- [26] Li Pang, Xiangyu Rui, Long Cui, Hongzhong Wang, Deyu Meng, and Xiangyong Cao. Hir-diff: Unsupervised hyperspectral image restoration via improved diffusion models. In *CVPR*, pages 3005–3014, 2024. 2, 7
- [27] Rakesh C. Patel and Manjunath V. Joshi. Super-resolution of hyperspectral images: Use of optimum wavelet filter coefficients and sparsity regularization. *IEEE TGRS*, 53(4):1728–1736, 2015. 2
- [28] Jiangjun Peng, Qi Xie, Qian Zhao, Yao Wang, Yee Leung, and Deyu Meng. Enhanced 3dtv regularization and its applications on HSI denoising and compressed sensing. *IEEE TIP*, 29:7889–7903, 2020. 2
- [29] Jiangtao Peng, Weiwei Sun, Heng-Chao Li, Wei Li, Xi-angchao Meng, Chiru Ge, and Qian Du. Low-rank and sparse

- representation for hyperspectral image processing: A review. *IEEE Geoscience and Remote Sensing Magazine*, 10(1):10–43, 2022. 1
- [30] Jiangjun Peng, Yao Wang, Hong-Ying Zhang, Jianjun Wang, and Deyu Meng. Exact decomposition of joint low rankness and local smoothness plus sparse matrices. *IEEE TPAMI*, 45(5):5766–5781, 2023. 2
- [31] Jiahui Qu, Yanzi Shi, Weiyang Xie, Yunsong Li, Xianyun Wu, and Qian Du. MSSL: hyperspectral and panchromatic images fusion via multiresolution spatial-spectral feature learning networks. *IEEE TGRS*, 60:5504113, 2022. 2
- [32] Xiangyu Rui, Xiangyong Cao, Li Pang, Zeyu Zhu, Zongsheng Yue, and Deyu Meng. Unsupervised hyperspectral pansharpening via low-rank diffusion model. *Inf. Fusion*, 107:102325, 2024. 2, 7
- [33] Yanli Shang, Jianjun Liu, Jingyi Zhang, and Zebin Wu. MFT-GAN: A multiscale feature-guided transformer network for unsupervised hyperspectral pansharpening. *IEEE TGRS*, 62:5518516, 2024. 1
- [34] Xin Tian, Wei Zhang, Yuerong Chen, Zhongyuan Wang, and Jiayi Ma. Hyperfusion: A computational approach for hyperspectral, multispectral, and panchromatic image fusion. *IEEE TGRS*, 60:1–16, 2022. 2
- [35] Hailin Wang, Jiangjun Peng, Wenjin Qin, Jianjun Wang, and Deyu Meng. Guaranteed tensor recovery fused low-rankness and smoothness. *IEEE TPAMI*, 45(9):10990–11007, 2023. 2
- [36] Wu Wang, Liang-Jian Deng, Ran Ran, and Gemine Vivone. A general paradigm with detail-preserving conditional invertible network for image fusion. *IJCV*, 132(4):1029–1054, 2024. 2
- [37] Xinya Wang, Jiayi Ma, and Junjun Jiang. Hyperspectral image super-resolution via recurrent feedback embedding and spatial-spectral consistency regularization. *IEEE TGRS*, 60:1–13, 2022. 2
- [38] Yao Wang, Jiangjun Peng, Qian Zhao, Yee Leung, Xi-Le Zhao, and Deyu Meng. Hyperspectral image restoration via total variation regularized low-rank tensor decomposition. *IEEE JSTARS*, 11(4):1227–1243, 2018. 2
- [39] Zhaoyang Wang, Dongyang Li, Mingyang Zhang, Hao Luo, and Maoguo Gong. Enhancing hyperspectral images via diffusion model and group-autoencoder super-resolution network. In *AAAI*, pages 5794–5804, 2024. 2
- [40] Kaixuan Wei, Ying Fu, and Hua Huang. 3-d quasi-recurrent neural network for hyperspectral image denoising. *IEEE TNNLS*, 32(1):363–375, 2021. 2
- [41] Chanyue Wu, Dong Wang, Yunpeng Bai, Hanyu Mao, Ying Li, and Qiang Shen. Hsr-diff: Hyperspectral image super-resolution via conditional diffusion models. In *ICCV*, pages 7060–7070, 2023. 2
- [42] Yi Xiao, Qiangqiang Yuan, Kui Jiang, Jiang He, Xianyu Jin, and Liangpei Zhang. Ediffsr: An efficient diffusion probabilistic model for remote sensing image super-resolution. *IEEE TGRS*, 62:5601514, 2024. 2
- [43] Fengchao Xiong, Jiantao Zhou, Jun Zhou, Jianfeng Lu, and Yuntao Qian. Multitask sparse representation model-inspired network for hyperspectral image denoising. *IEEE TGRS*, 61:5518515, 2023. 2
- [44] Shuang Xu, Jianshe Zhang, Zixiang Zhao, Kai Sun, Junmin Liu, and Chunxia Zhang. Deep gradient projection networks for pan-sharpening. In *CVPR*, pages 1366–1375, 2021. 6
- [45] Shuang Xu, Qiao Ke, Jiangjun Peng, Xiangyong Cao, and Zixiang Zhao. Pan-denoising: Guided hyperspectral image denoising via weighted represent coefficient total variation. *IEEE TGRS*, 62:5528714, 2024. 3, 7
- [46] Zhi-Qin John Xu, Yaoyu Zhang, and Tao Luo. Overview frequency principle/spectral bias in deep learning. *arXiv*, 2201.07395, 2022. 3
- [47] Qiangqiang Yuan, Qiang Zhang, Jie Li, Huanfeng Shen, and Liangpei Zhang. Hyperspectral image denoising employing a spatial-spectral deep residual convolutional neural network. *IEEE TGRS*, 57(2):1205–1218, 2019. 2
- [48] Haijin Zeng, Jie Zhang Cao, Kai Zhang, Yongyong Chen, Hiep Luong, and Wilfried Philips. Unmixing diffusion for self-supervised hyperspectral image denoising. In *CVPR*, pages 27820–27830, 2024. 2
- [49] Hongyan Zhang, Wei He, Liangpei Zhang, Huanfeng Shen, and Qiangqiang Yuan. Hyperspectral image restoration using low-rank matrix recovery. *IEEE TGRS*, 52(8):4729–4743, 2014. 2
- [50] Qiang Zhang, Yushuai Dong, Yaming Zheng, Haoyang Yu, Meiping Song, Lifu Zhang, and Qiangqiang Yuan. Three-dimension spatial-spectral attention transformer for hyperspectral image denoising. *IEEE TGRS*, 62:5531213, 2024. 1
- [51] Qiang Zhang, Yaming Zheng, Qiangqiang Yuan, Meiping Song, Haoyang Yu, and Yi Xiao. Hyperspectral image denoising: From model-driven, data-driven, to model-data-driven. *IEEE TNNLS*, 35(10):13143–13163, 2024. 1